IEEE Access
Multidisciplinary | Rapid Review | Open Access Journal

Received 10 August 2023, accepted 2 September 2023, date of publication 12 September 2023,
date of current version 15 September 2023.

Digital Object Identifier 10.1109/ACCESS.2023.3314505

RESEARCH ARTICLE

Super-Resolution for MRI Using Phase-Scrambling Fourier Transform Imaging and Unrolling Model-Based Network

KAZUKI YAMATO[1], (Member, IEEE), AND SATOSHI ITO[2], (Member, IEEE)
[1]Department of Fundamental Engineering, School of Engineering, Utsunomiya University, Utsunomiya 321-8585, Japan
[2]Department of Innovation Systems Engineering, Graduate School of Engineering, Utsunomiya University, Utsunomiya 321-8585, Japan

Corresponding author: Kazuki Yamato (yamato@is.utsunomiya-u.ac.jp)

This work was supported by a Grant for Young Exploratory Research in the School of Engineering, Utsunomiya University.

ABSTRACT Phase-scrambling Fourier transform imaging is an imaging technique for MRI and has useful features not found in Fourier transform imaging techniques generally used in MRI. In our previous study, an MR super-resolution method using a phase-scrambling Fourier transform signal was proposed. The previous method had two problems: a small improvement in resolution in the center regions of the reconstructed image and performance limitations in the iterative reconstruction. To solve these problems, here we propose an MR super-resolution method using a phase-scrambling Fourier transform signal and an unrolling model-based network. The proposed method utilizes Generic-ADMM-Net as the unrolling model-based network because MR super-resolution can be regarded as compressed sensing with image reconstruction from band-limited signals. To verify the effectiveness of the proposed method, we conducted simulation experiments. In the experiments, in addition to quantitative evaluation of the resolution improvement using numerical phantom images and reconstruction experiments using real-valued images, to evaluate the practical use of our method, we also conducted reconstruction experiments using noise-added images and complex images with phase components. As a result, it was confirmed that the images reconstructed from a Phase-Scrambling Fourier Transform (PSFT) signal had higher quality and better resolution improvement than those reconstructed from an FT signal. Moreover, the reconstruction performance of the proposed method outperformed that of the previous method, and the resolution of the center regions of the reconstructed image was improved. Furthermore, the results of practical experiments showed that the proposed method had a noise reduction effect and can be applied to complex images with phase components.

INDEX TERMS Deep learning, MRI, phase-scrambling Fourier transform, super resolution.

I. INTRODUCTION

Magnetic resonance imaging (MRI) is an in-vivo imaging technique that can safely acquire intravital information at high resolution. However, the imaging procedure in MRI takes a long time, such as several tens of minutes, because of the relaxation time. Therefore, acceleration of MRI is a critical issue. One approach to accelerating MRI is compressed sensing (CS) [1], [2], in which the original information can be recovered from a small number of measured signals that do not satisfy Shannon's sampling theorem, and this approach has been proposed for application to MRI in a scheme called compressed sensing-MRI (CS-MRI) [3], [4], [5], [6], [7]. CS-MRI can reduce the imaging time by under-sampling k-space signals according to CS. On the other hand, image reconstruction by CS-MRI is performed by iteratively solving the CS optimization problem. Hence, the computations required for the image reconstruction are high complex, and the quality of the image reconstructed with an iterative algorithm is limited.

On the other hand, imaging techniques using the quadratic field gradient have been studied by many researchers [8], [9], [10], [11], [12], [13], [14], [15], [16], [17], [18], [19],

The associate editor coordinating the review of this manuscript and approving it for publication was Prakasam Periasamy.

[20], [21], [22] and have useful features not found in general Fourier transform imaging (FT), such as reducing aliasing artifacts [8], [9], [10], improving dynamic range [11], [12], and superior image quality for CS [13], [14], [15]. As an example of the quadratic field gradient for CS, Puy et al. [13] proposed so-called spread spectrum MRI to accelerate single coil CS-MRI. This method consists of pre-modulating the signal by a linear chirp produced by the application of a quadratic phase profile, randomly under-sampling in k-space, and reconstructing the signal with non-linear optimization. Wang et al. [15] proposed a hybrid-encoding strategy with CS reconstruction which integrates Fourier encoding and Toeplitz encoding in 3D MRI. This method used a phase-scrambling RF excitation pulse to reduce the signal dynamic range, improving the SNR of the reconstructed image. Compared to other non-Fourier encoding methods, this method could obtain a comparative level of performance in preserving details. In addition, Zaitsev et al. [16] proposed a method for obtaining coil sensitivity information for parallel imaging solely from an under-sampled signal. In this method, the quadratic phase is imparted to the image to spread the k-space signal, and a window function can be introduced to the convolved chirp function. As a result, an alias-free image with no loss of image resolution can be obtained, and the necessity for acquisition of additional coil sensitivity information is avoided.

In a previous study related to the work in this paper, a super-resolution technique for MR imaging using PSFT imaging [11], [12] was proposed by Ito et al. [19], [20]. PSFT is an imaging technique for MRI that applies quadratic phase modulation to an object and one of the imaging methods using the quadratic field gradient. The super-resolution method proposed by Ito et al. uses an iterative algorithm similar to that proposed by Gerchberg [23] and extrapolates the low-resolution PSFT signal acquired from MRI. As a result, the spatial resolution of the reconstructed image is improved after acquiring MR signals. The iterative algorithm in the previous study is same as CS in terms of reconstructing the image from a small number of measured signals. The previous method does not sample the signal according to a specific sampling pattern such as Cartesian trajectories, but instead treats the bandwidth-limited area of the signal space as the sampling area. Therefore, the previous method can be considered to be a kind of acceleration of MRI. In addition, super-resolution methods for natural images [24], [25], [26] are generally based on optical imaging, and a high-resolution image is estimated by using the relationship between pixels in the image domain. On the other hand, the previous study is a super-resolution method based on a PSFT signal. Considering that MR images are obtained from k-space, the previous super-resolution method based on a PSFT signal is reliable and suitable for MR images. However, there are two problems: one is that the resolution improvement decreases from the marginal regions to the center regions of the reconstructed image, and the other is that there are limitations in the reconstruction performance of the iterative reconstruction as well as CS-MRI.

Incidentally, there have been studies to improve the reconstruction performance of CS-MRI by using deep learning, which has been the focus of much attention in recent years. Deep learning-based CS-MRI reconstruction methods can be categorized as unrolling model-based networks [27], [28], [29], [30], [31] and non-unrolling model-based networks [32], [33], [34], [35], [36]. The network architecture of an unrolling model-based network is constructed based on the steps resulting from the iterative optimization problem of CS, and parameters and functions included in the iteration steps are learned through network training. Generic-ADMM-Net proposed by Yang et al. [27] and ISTA-Net proposed by Zhang et al. [29] are classified as unrolling model-based networks. On the other hand, non-unrolling model-based networks use standard architectures that are designed for purposes other than reconstruction. The networks included in this category are U-Net proposed by Ronneberger et al. [32], DAGAN proposed by Yang et al. [33], and so on.

In this paper, we proposed a novel MR super-resolution method using a PSFT signal and an unrolling model-based network in order to solve the two problems with iterative super-resolution in our previous study. The iterative algorithm of the previous super-resolution method consists of iterative transforms between PSFT signal space and image space and replacement of the ground truth signal. Generic-ADMM-Net, which is an unrolling model-based network, has a layer that transforms between signal space and image space and is suitable for extending the previous iterative algorithm to deep learning. Note that since Generic-ADMM-Net is designed based on an FT signal whereas the proposed method uses a PSFT signal, it is necessary to modify Generic-ADMM-Net to deal with a PSFT signal. To verify the effectiveness of the proposed super-resolution, we conducted simulation experiments. As a result, the performance of reconstruction methods using the PSFT signal is higher than those using the FT signal. Moreover, the proposed method using deep learning was superior to the previous method based on an iterative algorithm with respect to the quantitative evaluation and the visual comparison of reconstructed images. In addition, the resolution improvement ratio was measured by numerical phantom images, and it was confirmed that the resolution of the image reconstructed by the proposed method was improved in not only the marginal area but also the central area.

II. PHASE-SCRAMBLING FOURIER TRANSFORM IMAGING

PSFT imaging is a technique in which a quadratic field gradient for the phase scrambling $\Delta B = b(x^2 + y^2)$ is added to the pulse sequence of conventional Fourier transform (FT) imaging in synchronization with a field gradient for phase encoding. The PSFT signal $v_{PSFT}(k_x, k_y)$ is represented

as follows:

$$v_{PSFT}(k_x, k_y) = \iint_{-\infty}^{\infty} \left\{\rho(x, y)e^{-j\gamma b\tau(x^2+y^2)}\right\} e^{-j(k_x x+k_y y)}dxdy$$
$$= F(\rho(x, y)e^{-j\gamma b\tau(x^2+y^2)}), \quad (1)$$

where $\rho(x, y)$ denotes the spin density distribution in the imaging object; k_x and k_y denote wave numbers of the PSFT signals, represented as $k_x = \gamma G_x t_x$ and $k_y = \gamma G_y t_y$, respectively; $\gamma b\tau$ is the phase scrambling parameter; γ, b, and τ are the gyromagnetic ratio, coefficient of the quadratic field gradient, and its impressing time, respectively; $F(\cdot)$ denotes the Fourier transform; G_x and G_y are the coefficients of the linear field gradients in the x and y directions, respectively; and t_x and t_y are the impressing times of G_x and G_y, respectively. $\rho(x, y)$ can be obtained by taking the inverse Fourier transform $F^{-1}(\cdot)$ of $v_{PSFT}(k_x, k_y)$ and multiplying the resulting signal by the quadratic phase term $e^{j\gamma b\tau(x^2+y^2)}$, as shown below:

$$\rho(x, y) = e^{j\gamma b\tau(x^2+y^2)}F^{-1}(v_{PSFT}(k_x, k_y)). \quad (2)$$

Consider the normalization of the phase scrambling parameter $\gamma b\tau$. For simplicity, only the x direction is considered. When the number of data is N, and the pixel width is Δx, the phase scrambling parameter that satisfies the sampling theory in x direction is represented by:

$$\overline{\gamma b\tau} = \frac{\pi}{N\Delta x^2}. \quad (3)$$

Therefore, the phase scrambling parameter is represented by $\gamma b\tau = h\overline{\gamma b\tau}$ by introducing the phase scrambling coefficient h. Note that $\gamma b\tau$ in the y direction is different from that in the x direction in cases where $\Delta x \neq \Delta y$, and the number of data is different between the x and y directions. Note that the PSFT of $h = 0$ is equivalent to FT.

III. SUPER-RESOLUTION BASED ON PSFT SIGNAL

A. RESOLUTION IMPROVEMENT BY AMPLITUDE MODULATED SIGNAL

Consider that an image is reconstructed from the amplitude modulated signal under the condition that the object is a real-valued function. The procedure for the reconstruction from the amplitude modulated signal is shown in Fig. 1. Suppose that the spin density distribution and its Fourier transformed function are $\rho(x)$ and $R(k)$, respectively. First, the amplitude modulation of frequency k_0 is applied to the object, and the amplitude modulated object $\rho(x)e^{jk_0x}$ can be obtained as shown in Fig. 1(a). Then, a Fourier transform is applied to $\rho(x)e^{jk_0x}$, and the amplitude modulated signal $R(k - k_0)$ is obtained according to the modulation property of the Fourier transform, as shown in Fig. 1(b). Here, the rectangular function $\mathrm{rect}(k/k_w)$ with width k_w is applied to $R(k - k_0)$ to acquire the band-limited signal $\mathrm{rect}(k/k_w)R(k-k_0)$, as shown in Fig.1(c). The reconstructed image $\rho_{\mathrm{band}}(x)$ obtained by applying the inverse Fourier transform and amplitude

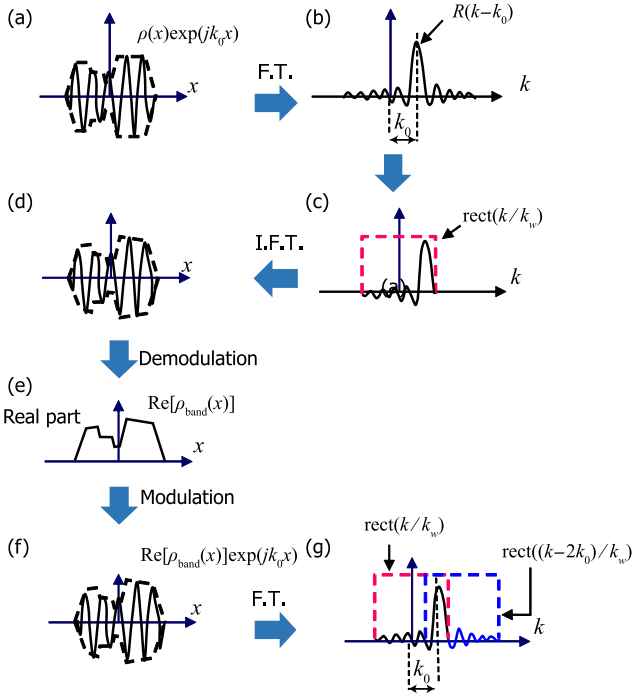

FIGURE 1. Principle of frequency bandwidth expansion of amplitude modulated image. The frequency bandwidth of an amplitude modulated image can be expanded when a target object is treated as a real-valued function.

demodulation to $\mathrm{rect}(k/k_w)R(k - k_0)$, is as follows:

$$\rho_{\mathrm{band}}(x) = e^{-jk_0x}F^{-1}\left[\mathrm{rect}\left(\frac{k}{k_w}\right)R(k - k_0)\right]$$
$$= e^{-jk_0x}\left[\rho(x)e^{jk_0x} * \mathrm{sinc}(k_w x)\right] \quad (4)$$

Because the target object is a real-valued function, the real part of $\rho_{\mathrm{band}}(x)$ shown in Fig. 1(e) is extracted as follows:

$$\mathrm{Re}\left[\rho_{\mathrm{band}}(x)\right] = \mathrm{Re}\left[e^{-jk_0x}\left\{\rho(x)e^{jk_0x} * \mathrm{sinc}(k_w x)\right\}\right]$$
$$= \frac{1}{2}[e^{-jk_0x}\{\rho(x)e^{jk_0x} * \mathrm{sinc}(k_w x)\}$$
$$+ e^{jk_0x}\{\rho(x)e^{-jk_0x} * \mathrm{sinc}(k_w x)\}] \quad (5)$$

As shown in Fig. 1(f), the amplitude modulation using e^{jk_0x} and the Fourier transform are applied to the real part of ρ_{band} as follows:

$$F\left[\mathrm{Re}[\rho_{\mathrm{band}}(x)]e^{jk_0x}\right]$$
$$= \frac{1}{2}[F[\rho(x)e^{jk_0x} * \mathrm{sinc}(k_w x)]$$
$$+ F[e^{j2k_0x}\{\rho(x)e^{-jk_0x} * \mathrm{sinc}(k_w x)\}]]$$
$$= \frac{1}{2}\left[\mathrm{rect}\left(\frac{k}{k_w}\right)R(k - k_0) + \mathrm{rect}\left(\frac{k - 2k_0}{k_w}\right)R(k - k_0)\right]. \quad (6)$$

The above equation represents that the signal bandwidth is expanded from k_w to $k_w + 2k_0$ when the signal amplitude of the overlapping region of two rectangular functions is halved, as shown in Fig. 1(g).

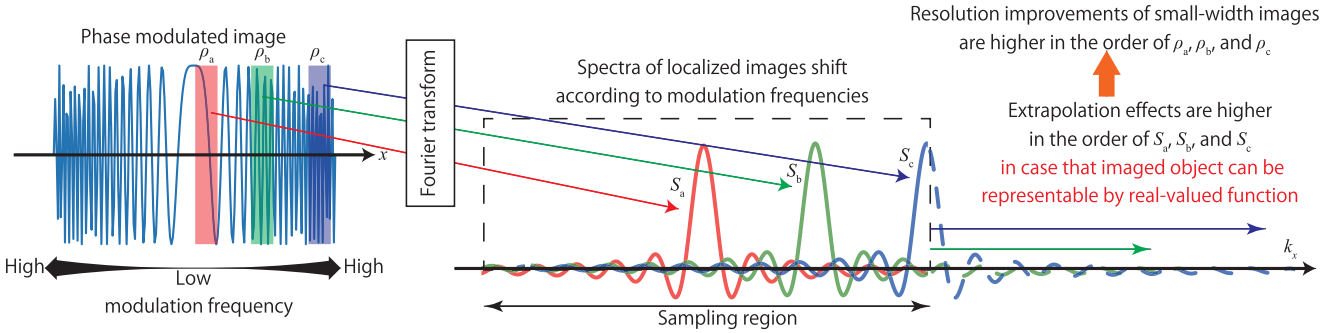

FIGURE 2. Super-resolution principle of PSFT signal. ρ_a, ρ_b, and ρ_c are small-width images with quadratic phase modulation. The modulation frequencies are higher in the order of ρ_a, ρ_b, and ρ_c. The spectra obtained by applying a Fourier transform to those small-width images are S_a, S_b, and S_c. Each spectrum is shaped symmetrically with respect to the peak, and the peak position of each spectrum shifts with modulation frequency. The spectra outside the sampling region can be estimated by extrapolation using the symmetrical feature of the spectra. The extrapolation effect is higher for larger shifts, and it is increases in the order S_a, S_b, and S_c in this figure. Accordingly, the resolution improvements of the small-width images are also increase in the order ρ_a, ρ_b, and ρ_c.

B. SUPER-RESOLUTION PRINCIPLE BY PSFT SIGNAL

In PSFT, the spatio-temporal frequency of the image function increases with increasing distance from the origin of the image space because the phase of the object shifts quadratically in the x and y directions, i.e.,

$$\rho(x, y)e^{-j\gamma b\tau(x^2+y^2)} = \rho(x, y)e^{-j\{\omega(x)x+\omega(y)y\}}, \qquad (7)$$

where $\omega(x) = \gamma b\tau x$ and $\omega(y) = \gamma b\tau y$. Therefore, the signal bandwidth expansion described in III-A can be applied to the PSFT signal as a function with locally changing frequency. Since the frequency of amplitude modulation increases in proportion to the values of the xy spatial coordinates, the bandwidth expansion and corresponding resolution improvement are not uniform spatially but increase in proportion to the distance from the center of the image when the center of the quadratic field gradient is the center of the image.

Consider the localized small-width images ρ_a, ρ_b, and ρ_c shown in Fig. 2. The spatial frequency spectra of the small-width images S_a, S_b, and S_c shift in k_x-space in accordance with the modulation frequencies $\omega_x(x)$ and $\omega_y(y)$, as shown in Fig. 2. $\omega_x(x)$ and $\omega_y(y)$ increase with increasing distances from the center x and y in the image domain, respectively. When the imaged object is assumed to be representable by a real-valued function, the spectrum can be extrapolated to make it symmetric with its peak, which resembles the half Fourier encoding method, as shown in Fig. 2, which improves the spatial resolution. The resolution improvement depends on the distance from the center of the quadratic phase function applied to the imaged object.

The iterative algorithm of signal extrapolation for the PSFT signal is shown in Fig. 3. This algorithm is based on Gerchberg's iterative algorithm. First, the PSFT signal with N data points is acquired from MRI, and the area outside of the acquired signal is filled with zero values to form $2N$ points, as shown in Fig. 3(a). Then, the inverse Fourier transform is applied to the zero-filled PSFT signal. Since the obtained image shown in Fig. 3(b) is modulated by the quadratic phase, the quadratic phase demodulation should be applied to the obtained image. In addition, the reconstructed image can be

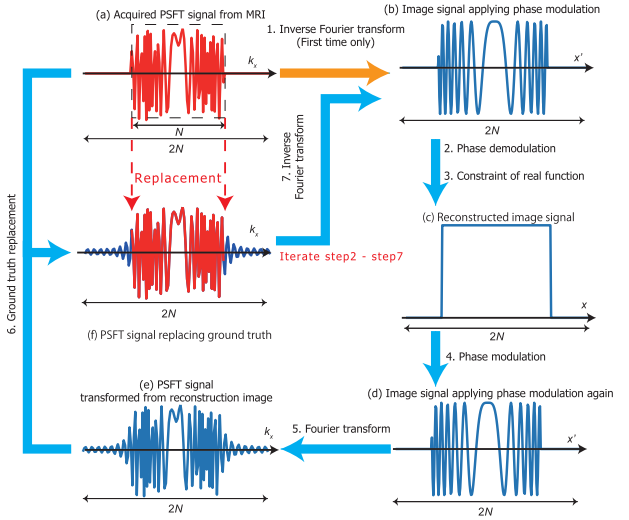

FIGURE 3. Flow of iterative signal extrapolation algorithm. This figure represents an example of a rectangular function as a target object.

obtained using the constraint that the target object can be represented in the real value function, as shown in Fig. 3(c). Next, the PSFT signal is calculated from the reconstructed image as shown in Fig. 3(d) and (e). The obtained PSFT signal in Fig. 3(e) is expanded in the frequency band that is zero-filled in Fig. 3(a). Since there are ground truth values with respect to N data points of the center of the PSFT signal, the N data points of the center of the PSFT signal can be replaced by the acquired PSFT signal as the ground truth, as shown in Fig. 3(f).

After the replacement of the PSFT signal, the inverse Fourier transform is applied to the replaced PSFT signal. In this algorithm, steps 2 to 7 in Fig. 3 are iterated.

IV. PSFT-COMPATIBLE GENERIC-ADMM-NET

The super-resolution using a PSFT signal described above can obtain a high-resolution image from a low-resolution image by extrapolating signals outside the sampling region when the imaged object can be represented by a real-valued function. In other words, it can be regarded as a

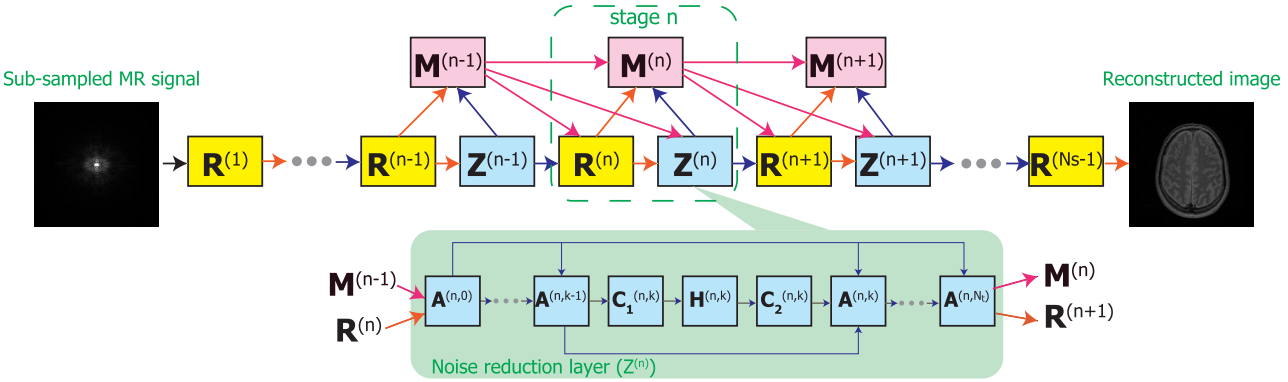

FIGURE 4. The data flow graph for Generic-ADMM-Net. $\mathbf{R}^{(n)}$, $\mathbf{Z}^{(n)}$, and $\mathbf{M}^{(n)}$ represent the n-th reconstruction layer, the n-th noise reduction layer, and the n-th multiplier update layer, respectively, and the n-th stage consists of these layers. The layer $\mathbf{Z}^{(n)}$ is decomposed to N_t iterations consisting of convolution layers $\mathbf{C}_1^{(n,k)}$, $\mathbf{C}_2^{(n,k)}$, non-linear activation layers $\mathbf{H}^{(n,k)}$, and addition layers $\mathbf{A}^{(n,k)}$, where $k \in \{1, 2, \ldots, N_t\}$. In this paper, the rectified linear unit (ReLU) is substituted as the non-linear activation layers, and N_t equals 1 in order to decrease the computational costs of network training.

compressed sensing that estimates a large amount of signals from a small amount of signals. Hence, the optimization technique of compressed sensing can be applied to the proposed super-resolution technique. Recently, unrolling-based deep learning in which the parameters of an optimization problem are trained was proposed and achieved a high level of performance that exceeded that of the conventional iterative optimization. In this study, Generic-ADMM-Net, which is an unrolling-based network, is applied to the proposed super-resolution to increase the resolution improvement effect over iterative algorithms. On the other hand, the proposed method is not based on an FT signal but a PSFT signal. Therefore, a PSFT-compatible Generic-ADMM-Net in which the network layers of Generic-ADMM-Net are modified to be able to input an PSFT signal is constructed in this paper.

The generic-alternating direction method of multipliers (ADMM) network proposed by Yang et al. was designed by employing unrolling ADMM optimization [37], [38] to train the regularization parameters of CS-MRI with respect to a PSFT signal. In the CS-MRI model, the reconstructed image ρ is estimated by solving the optimization problem as follows:

$$\hat{\boldsymbol{\rho}} = \arg\min_{\boldsymbol{\rho}} \left\{ \frac{1}{2}\|\mathbf{PFS}\boldsymbol{\rho} - \mathbf{m}\|_2^2 + \sum_{l=1}^{L} \lambda_l g(\mathbf{D_l}\boldsymbol{\rho}) \right\}, \tag{8}$$

where $\mathbf{m}$ is a truncated and sampled signal, $\mathbf{P}$ is a truncated function, $\mathbf{S} = e^{-j\gamma b\tau(x^2+y^2)}$ is the quadratic phase modulation term, $\mathbf{F}$ is the Fourier transform, $\mathbf{D_l}$ denotes an undetermined linear transform, $g(\cdot)$ is a nonlinear regularization function, and λ_l is a regularization parameter.

By introducing the independent auxiliary variables $\mathbf{z} = \{\mathbf{z}_1, \mathbf{z}_2, \ldots, \mathbf{z}_L\}$ in the image domain and using the Lagrangian multiplier β, the iterations of the ADMM algorithm are represented as follows:

$$\begin{cases} \arg\min_{\boldsymbol{\rho}} \dfrac{1}{2}\|\mathbf{PFS}\boldsymbol{\rho} - \mathbf{m}\|_2^2 - \dfrac{r}{2}\|\boldsymbol{\rho} + \boldsymbol{\beta} - \mathbf{z}\|_2^2, \\ \arg\min_{\mathbf{z}} \displaystyle\sum_{l=1}^{L} \lambda_l g(\mathbf{D}_l\mathbf{z}) + \dfrac{r}{2}\|\boldsymbol{\rho} + \boldsymbol{\beta} - \mathbf{z}\|_2^2, \\ \boldsymbol{\beta} \longleftarrow \boldsymbol{\beta} + \tilde{\eta}(\boldsymbol{\rho} - \mathbf{z}), \end{cases} \tag{9}$$

where the parameter $\tilde{\eta}$ is an update rate, and r is a penalty parameter. Letting I be a unit matrix, these iterations have the following solutions:

$$\begin{cases} \mathbf{R}^{(n)} : \boldsymbol{\rho}^{(n)} = \mathbf{S}^*\mathbf{F}^T \dfrac{\left[\mathbf{P}^T\mathbf{y} + r\mathbf{FS}(\mathbf{z}^{(n-1)} - \boldsymbol{\beta}^{(n-1)})\right]}{(\mathbf{P}^T\mathbf{P} + r\mathbf{I})}, \\ \mathbf{Z}^{(n)} : \mathbf{z}^{(n,k)} = \mu_1\mathbf{z}^{(n,k-1)} + \mu_2(\boldsymbol{\rho}^{(n)} + \boldsymbol{\beta}^{(n-1)}) \\ \qquad - \displaystyle\sum_{l=1}^{L} \lambda_l \mathbf{D}_l^T \mathcal{H}(\mathbf{D}_l\mathbf{z}^{(n,k-1)}), \\ \mathbf{M}^{(n)} : \boldsymbol{\beta}^{(n)} = \boldsymbol{\beta}^{(n-1)} + \tilde{\eta}(\boldsymbol{\rho}^{(n)} - \mathbf{z}^{(n)}), \end{cases} \tag{10}$$

where $\mathbf{S}^*$ denotes the complex conjugate of $\mathbf{S}$, $\mathcal{H}(\cdot)$ refers to a non-linear transform corresponding to the gradient of the regularization function $g(\cdot)$, and k denotes the k-th sub-iteration of $\mathbf{z}^{(n)}$. In the solution Z, $\mu_1 = 1 - \delta r$, $\mu_2 = \delta r$, $\lambda_l = \delta\lambda_l$ where δ is the step size in the gradient descent method. In the iteration of the ADMM algorithm, the solutions represented in (10) are alternately updated in the order of $\mathbf{R}^{(n)}$, $\mathbf{Z}^{(n)}$, and $\mathbf{M}^{(n)}$.

Figure 4 shows the data flow graph of Generic-ADMM-Net. As shown in Fig. 4, the n-th stage in the data flow graph corresponds to the n-th iteration of the ADMM algorithm. In Generic-ADMM-Net, the solutions of (10), that is, $\mathbf{R}$, $\mathbf{Z}$, and $\mathbf{M}$, act as three kinds of layers. The layers $\mathbf{R}$, $\mathbf{Z}$, and $\mathbf{M}$ are the reconstruction layer, noise reduction layer, and multiplier update layer, respectively, and a set of these layers is treated as a stage, which is equivalent to a solving step of the ADMM algorithm in (10). Generic-ADMM-Net

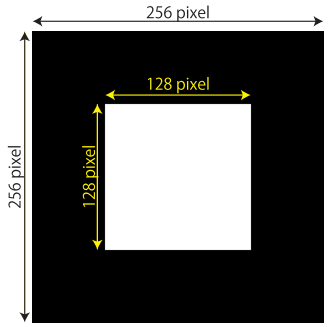

FIGURE 5. Band limitation used in the experimental simulations. The signals located in the white region are under-sampled, and the black region is extrapolated by the reconstruction methods.

trains the penalty parameter r in the reconstruction layers, the convolution filter of the convolution layers $\mathbf{C}_1$ and $\mathbf{C}_2$, which are sub-layers of the noise reduction layers $\mathbf{Z}$, the multiplier update parameter $\tilde{\eta}$, and the regularization parameter λ_l. The difference between Generic-ADMM-Net and PSFT-compatible Generic-ADMM-Net is only the reconstruction layers in which a PSFT signal can be input. Therefore, the network structure of PSFT-compatible Generic-ADMM-Net is identical to that of Generic-ADMM-Net.

In the training of Generic-ADMM-Net, a training dataset consists of a pair of an under-sampled FT signal and the ground-truth image. A training dataset of PSFT-compatible Generic-ADMM-Net is a pair of an under-sampled PSFT signal and the ground truth image. In the training of both ADMM-Nets, under-sampled signals are input to the network and the loss between the reconstructed image output from the network and the ground-truth image is calculated. Generic-ADMM-Net uses the normalized mean squared error (NMSE) as the loss function and PSFT-compatible Generic-ADMM-Net also uses NMSE.

V. EXPERIMENTAL RESULTS

A. EXPERIMENTAL CONFIGURATION

To verify the effectiveness of the proposed method, we conducted experimental simulations. In the simulations, the signals obtained by applying the band limitation shown in Fig. 5 to PSFT signals calculated from existing MR images were regarded as the signals acquired from the MRI. Four kinds of the experiments are described in this section. The results from the first experiment are used to evaluate the resolution improvement of the reconstructed image quantitatively. The other experimental results are the reconstruction results from real-valued images, noise-added images, and complex images. In the resolution improvement and the reconstructions from real-valued images and noise-added images, 570 T1-weighted MR images of the heads of volunteers who gave consent, from the IXI Dataset [39]. 400 randomly selected images were used for training, and the rest were used for testing. In the reconstructions from complex images, we used 144 T1-weighted images provided in the fastMRI dataset [40], of which 100 randomly selected images were used for training and the rest for testing. All images were 256×256 pixels. In addition, the experimentally obtained PSFT signal was also used in order to demonstrate the practical applicability of the proposed method. The used experimental data was acquired by magnetic field intensity 0.2 T MRI. The quadratic field gradient for PSFT was realized by the coil system designed for the quadratic field gradient. As the imaging conditions, the signal matrix size was 256×256, the resolution was $\delta_x = \delta_y = 0.035$ cm, and $\gamma b\tau = 10.0$ rad/cm^2. The imaging object was Yuzu.

In the settings of PSFT-compatible Generic-ADMM-Net, the input size, the number of epochs, the non-linear activation layer, and the optimizer were set to 256×256, 300, Rectified Linear Unit (ReLU) [41], and Adam [42], respectively. In the quantitative evaluation of the reconstructed images, the peak signal-to-noise ratio (PSNR) and the structural similarity index measure (SSIM) [43] were used. The experimental simulations were conducted on a computer with an Intel(R) Core(TM) i9-11900K CPU (3.5 GHz), 64 GB of RAM, and an NVIDIA GeForce RTX 3090 GPU running Windows 10. The software used was Python 3.7.9, PyTorch 1.11.0, CUDA ToolKit 11.3. The training times under the above configurations were about 45 minutes.

Note that PSFT-compatible Generic-ADMM-Net is denoted by PSFT-ADMM-Net, and Generic-ADMM-Net using an FT signal is denoted by FT-ADMM-Net in the experimental results. The methods compared with PSFT-ADMM-Net were iterative SR shown in Fig. 3 and C-SALSA-B [44], which is a CS optimization algorithm. The number of iterations for both methods was set to 100.

In the resolution improvement evaluation, a standard numerical phantom shown in Fig. 6(b) was used to evaluate the resolution improvement of the reconstructed images quantitatively. The criterion for quantitative resolution improvement was the amplitude ratio of a slit in the reconstructed phantom, which was compared to that of FT. As a result, the resolution improvement ratio was calculated from the amplitude ratios of the slits. The amplitude ratio p_{ar} was calculated as follows:

$$p_{ar} = \frac{B_n - B}{B_n}, \tag{11}$$

where B_n and B denote the mean amplitude value around the slit, and the amplitude value of the slit, respectively. When $p_{ar} = 1$, the resolution improvement effect was the maximum. To calculate the resolution with respect to FT from the amplitude ratio of the reconstructed slit, band limitation was applied to the FT signal, and the resolution reference line was created as shown in Fig. 6(c). The band limitation ratio S shown in Fig. 6(c) corresponds to the size of the band limitation region. The band limitation when $S = 1$ is that the signal of a 256×256-sized numerical phantom is zero-filled except for the 128×128 center region. The amplitude ratio was calculated by changing S, and its distribution was approximated. As a result, a resolution reference line can be obtained as shown in Fig. 6(c). Note that when $S = 2$, $p_{ar} = 1$ because band limitation was not applied. The models

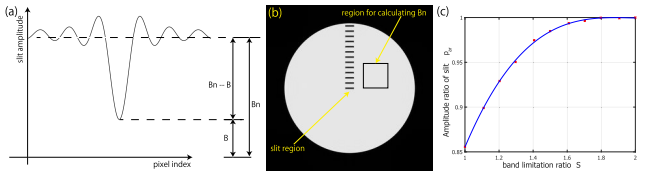

FIGURE 6. Settings for resolution improvement evaluation. (a) depicts the amplitude of the slit, and (b) shows a standard numerical phantom used in this experiment and indicates the slit region and a region for calculating B_n. (c) shows the resolution reference line obtained by calculating the amplitude ratio while changing S. (c) is approximated by a cubic formula.

of PSFT-ADMM-Net and FT-ADMM-Net for reconstructing the numerical phantom were trained with 400 T1-weighted MR images provided in the IXI Dataset.

In the experiment using real-valued MR images, the reconstructed images were generated by the models trained in the resolution improvement evaluation. The images used for the reconstruction were 170 T1-weighted MR images, with the exception of 400 images for training.

For more practical simulation conditions, the reconstruction experiments were conducted on noise-added images. The effects on the reconstructed images were verified by assuming that noise was introduced into the MR signal acquired from MRI. The noise-added images used in the experiments were created by adding white gaussian noise to PSFT or FT signals of the MRI image. Here, the added noise was adjusted so that the standard deviation of white gaussian noise σ was 0.025 and 0.050 relative to the maximum amplitude of the target signal. In this experiment, noise was added to the signal generated from the 570 MR images used in the above two experiments. 400 images were used for training and the rest for reconstruction experiments. The images selected for the training and reconstruction experiments were the same as in the above two experiments.

The image acquired from MRI is a complex image that includes a spatial phase distribution. To verify the reconstruction performance of the proposed method on complex images, reconstruction simulations using complex images were conducted. Note that the resolution improvement effect of PSFT is the requirement that the subject can be represented by real values. However, complex images cannot satisfy this requirement. To solve this restriction, the spatial phase distributions of complex images are estimated and corrected for converting complex images to real-valued images.

In general, the spatial phase distribution can be estimated from the low band signal of a complex image by applying band limitation to the MR signal. In the case of the PSFT signal, the band limitation for estimating the spatial phase distribution results in loss of marginal regions of the reconstructed image because the phase distribution of the PSFT signal approximately corresponds to the distribution in image space. In this study, we utilized the feature that a signal described by the formula of the Fresnel transform can be transformed by applying a quadratic phase modulation to the PSFT signal. Here, this quadratic phase modulation is called a Fresnel modulation. The band limitation of the PSFT

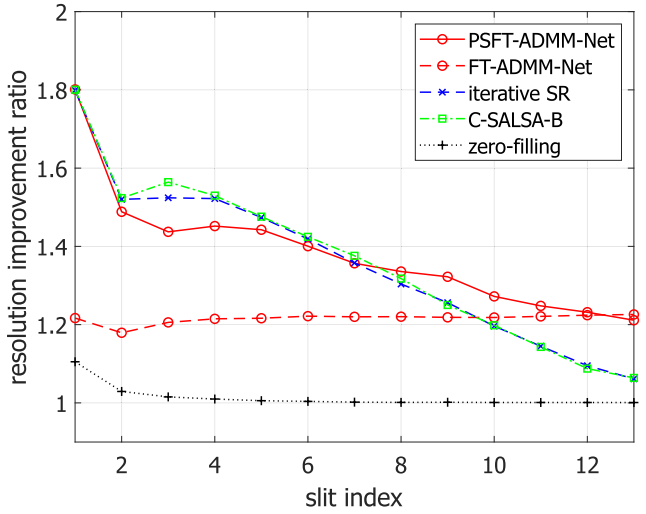

FIGURE 7. Resolution improvement ratio calculated from the amplitude ratio of slits. Slit index denotes indices of slits included the standard numerical phantom shown in Fig. 6. When the slit index is 1, the slit is located in the most marginal region. In contrast, the slit index of 13 indicates a slit located at the center of the phantom. Red solid and red dashed lines show the resolution improvement ratio of reconstructions from a PSFT signal and an FT signal by Generic-ADMM-Net, respectively. Blue and green dashed lines show iterative SR and C-SALSA-B as comparative methods, respectively. In this figure, zero-filling and FT-ADMM-Net use FT signals for the image reconstruction, and the phantom images are reconstructed from the PSFT signal and $h = 1.0$.

signal for estimating the spatial phase distribution is performed on the PSFT signal with a Fourier transform applied after the Fresnel modulation. In this experiment, we used 144 T1-weighted images provided in the fastMRI dataset [40], of which 100 randomly selected images were used for training and the rest for testing.

B. RESOLUTION IMPROVEMENT EVALUATION

Fig. 7 shows the measurement results of the resolution improvement ratio of the reconstructed slits. In this graph, zero-filling shows the resolution improvement ratio when the FT signal of the numerical phantom is applied to the band limitation according to Fig. 5. As shown in Fig. 7, the resolution improvement ratio of the methods using the PSFT signal, that is, PSFT-ADMM-Net, iterative SR, and C-SALSA-B, are higher than that of FT-ADMM-Net when the slit index is less than 12. Compared to the methods using the PSFT signal, the resolution improvement of PSFT-ADMM-Net is almost equal to that of iterative-based methods such as iterative SR and C-SALSA-B when the slit index is less than 8. When the slit index is more than 8, the iterative-based methods have significantly decreased resolution improvement ratios, in contrast to PSFT-ADMM-Net, which suppresses the decrease in the resolution improvement ratio.

C. SUPER-RESOLUTION RESULTS APPLIED TO REAL-VALUED IMAGES AND NOISE-ADDED IMAGES

In this section, the reconstruction results are shown for real-valued MR images. Fig. 8 shows the loss values of each epoch in the training phase of PSFT-ADMM-Net

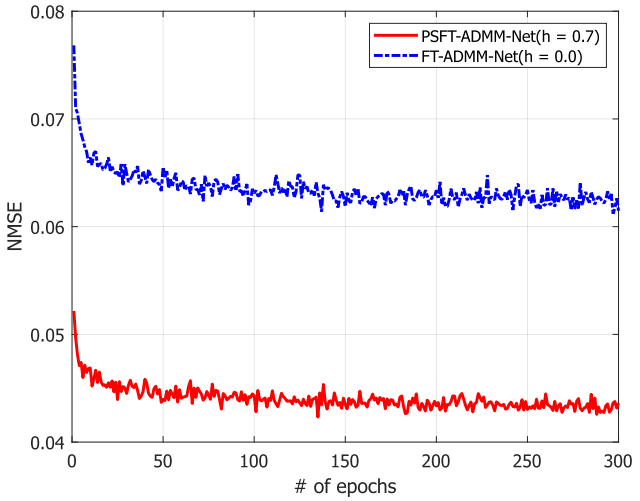

FIGURE 8. Loss values with respect to epochs. The loss functions of both PSFT-ADMM-Net and FT-ADMM-Net are the normalized mean squared error (NMSR).

and FT-ADMM-Net and Fig. 9 shows the reconstructed T1-weighted images. As shown in this figure, it is clear that the reconstructed images from the PSFT signal have higher quality than zero-filling from the FT signal. This is especially noticeable in the marginal region indicated by the yellow arrow and the central region indicated by the green arrow. In comparison to the iteration-based reconstruction and the deep learning-based reconstruction from the PSFT signal, the reconstructed image with iteration SR and C-SALSA-B contain noise-like artifacts but have improved resolution. On the other hand, the reconstructed image with PSFT-ADMM-Net shows better resolution than zero-filling and less noise than the iterative method. Although the reconstructed image with FT-ADMM-Net also contains less noise, the resolution improvement with FT-ADMM-Net is low. In comparison to error maps shown in the bottom rows of Fig. 9, it was confirmed that the error values of PSFT-ADMM-Net were smaller than the other error maps and were especially noticeable in the contour region.

As a quantitative evaluation, the measurement results of PSNR and SSIM of the reconstructed images are shown in Fig. 10. Here, ADMM-Net indicated by the red line corresponds to FT-ADMM-Net when $h = 0$ and to PSFT-ADMM-Net when $h > 0$. In the same manner, PSNR and SSIM of iterative SR and C-SALSA-B at $h = 0$ denote the evaluation results of reconstructed images from the FT signal with iterative SR and C-SALSA-B, respectively. As shown in Fig. 10, both PSNR and SSIM of the reconstructed images with ADMM-Net are higher than iterative SR and C-SALSA-B regardless of h. Comparing the reconstructed results from the FT signal and PSFT signal, both PSNR and SSIM of the reconstructed images from the PSFT signal are higher than those with the FT signal in all reconstruction methods. Therefore, PSNR and SSIM of the reconstructed image from the PSFT signal with Generic-ADMM-Net are the highest in all of the simulation conditions. In addition, the PSFT signals of the reconstructed images are shown in Fig. 11 The signals indicated by the profiles in this figure are the signals estimated by the reconstruction methods. In comparison to Fig. 11(d), it was confirmed that the reconstructed PSFT signals with the proposed method shown in Fig. 11(f) could be estimated more accurately than those of iterative SR.

Figure 12 shows the reconstructed images from noise-added images. In comparison to zero-filling reconstructed from the FT signal and reconstructed images from the PSFT signal, the resolution of zero-filling shows little improvement, and residual noise is visible. The reconstructed images with iterative SR and C-SALSA-B show an improvement in resolution even under the influence of noise. However, loss of detail due to residual noise is observed in the region indicated by the yellow arrow. On the other hand, the reconstructed image with PSFT-ADMM-Net is less noisy than that of the iterative methods, and the resolution improvement effect can be confirmed. In contrast, FT-ADMM-Net also has a noise reduction effect but a small resolution improvement.

Figure 13 shows PSNRs and SSIMs of the reconstructed images from noise-added images. From Fig. 13(a), the PSNRs of PSFT-ADMM-Net are higher than other methods regardless of the standard deviation σ of the white gaussian noise. On the other hand, the SSIMs of PSFT-ADMM-Net as well as FT-ADMM-Net are higher than other methods regardless of σ, and SSIM of PSFT-ADMM-Net is almost equal to that of FT-ADMM-Net.

D. SUPER-RESOLUTION RESULTS APPLIED TO COMPLEX IMAGES INCLUDING PHASE COMPONENTS

Figure 14 shows the reconstruction results of complex images. As shown in this figure, zero-filling from the FT signal contains zipper artifacts. The reconstructed images with iterative SR and C-SALSA-B show artifacts enhancing the zipper artifacts in the zero-filling. In contrast, the reconstructed images with FT-ADMM-Net and PSFT-ADMM-Net have no noticeable artifacts such as those in iteration-based methods. In addition, PSFT-ADMM-Net has better reproducibility of detailed structure than FT-ADMM-Net. From the above results, it was confirmed that the proposed PSFT-ADMM-Net is also effective for complex images including phase components.

VI. DISCUSSION

As shown in Fig. 2, the resolution of reconstructed images from the PSFT signal with iterative methods improves from the center of the image to its marginal regions. From the result in V-B, the resolution improvement effect of the iterative reconstructions such as iterative SR and C-SALSA-B was the highest at the marginal region and decreased toward the center of the image. This result is consistent with the super-resolution principle of PSFT. On the other hand, it was confirmed that the resolution improvement effect of PSFT-ADMM-Net was the highest at the marginal region, as with the iterative methods, whereas that at the center of the image

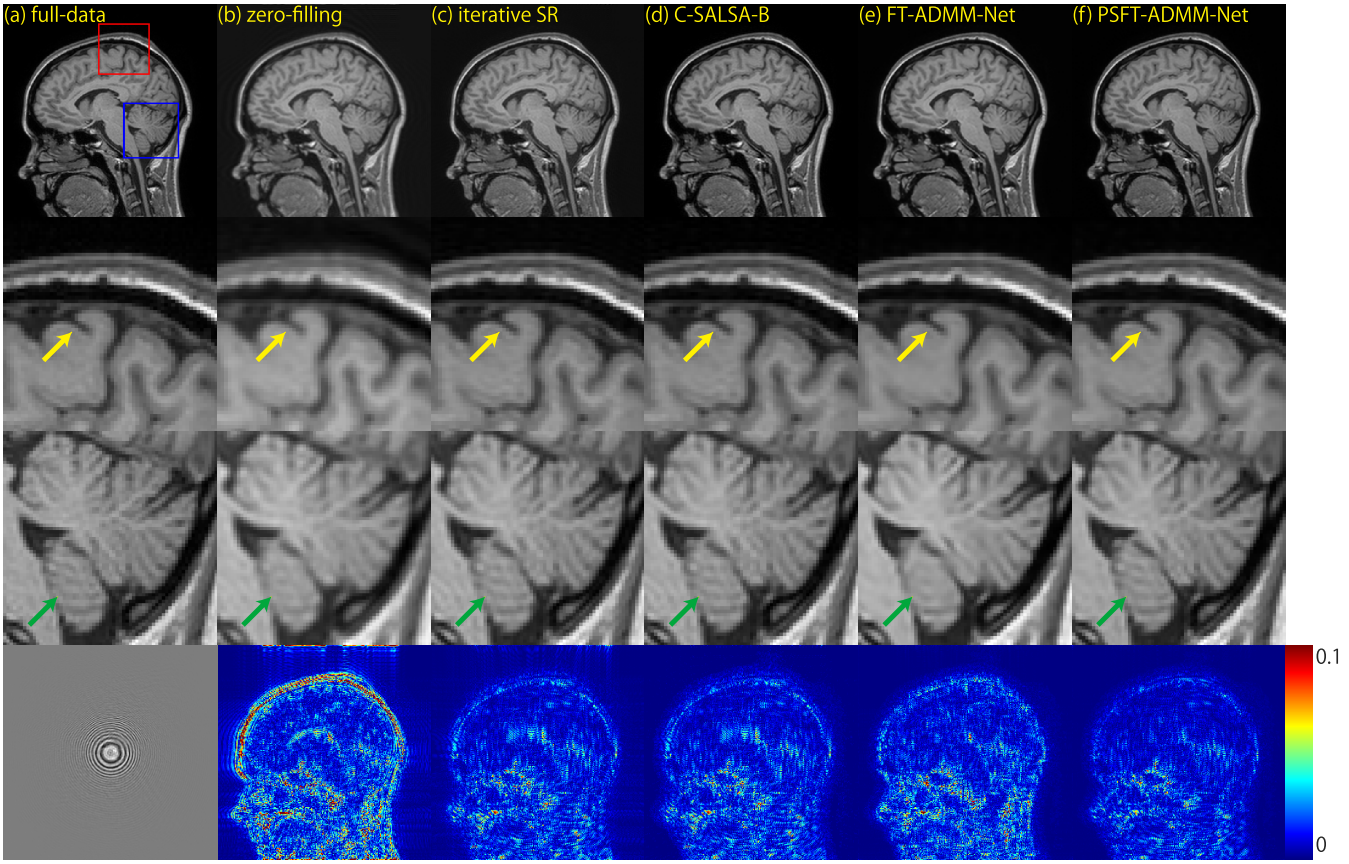

FIGURE 9. T1 weighted images reconstructed by each reconstruction method. The 1st row shows full-sized reconstructed images, the 2nd and 3rd rows are enlarged views of the red and blue rectangles in the full-data image, respectively. The last row shows the PSFT signal of the full data and the error maps between the full data and each reconstructed image. In this figure, the images are reconstructed from PSFT signals with $h = 0.7$ except (e); (e) is reconstructed from an FT signal, that is, $h = 0$.

was also improved to a certain degree. The reason for this is that the PSFT signal makes it possible to achieve higher resolution in the reconstructed image, and in addition, the band-limited high-frequency components of the image can be estimated with high accuracy by deep learning. In addition, the FT signal used generally in MRI concentrates energy in the center of the signal space. In contrast, the PSFT signal has a shape spread over the signal space according to the phase-scrambling coefficient h. Therefore, the shape of the PSFT signal has features that are easy to estimate with deep learning, so that a higher resolution reconstruction could be achieved compared with using the FT signal.

In the reconstructed results using real-valued images, the higher the phase-scrambling coefficient h is, the higher PSNR and SSIM are. They are the highest when $h = 0.7$. The same tendency is observed for methods using the PSFT signal regardless of the reconstruction method. h is a parameter that controls the scrambling range of the PSFT signal; the larger h is, the wider the PSFT signal is scrambled. As shown in Fig. 2, the wider the PSFT signal is scrambled, the higher the resolution improvement effect is. When h is a large value such as $h = 0.7$, the resolution of the reconstructed images from the PSFT signal is improved higher and higher. Concomitantly, the PSNR and SSIM of the reconstructed image are also high.

On the other hand, the PSNR and SSIM decrease for $h > 0.7$. In this experiment, T1-weighted sagittal MR images are used and contain a cross-sectional image of the neck at the bottom edge of the image. Theoretically, the larger h is, the higher the resolution improvement effect by the PSFT signal is. However, when the target object occupies the entire field of view, like the used T1-weighted images, it is difficult to recover the high-frequency signals by signal extrapolation. As a result, the reconstructed image has vignetting that occurs in the optical image sensor, such as cameras, and blurring occurs at the marginal regions of the reconstructed image. In the experimental results, the neck part of the used image is vignetted and blurred for the above reasons, and PSNR and SSIM are considered to be decreased.

As shown in Fig. 9 and 10, the reconstructed results using Generic-ADMM-Net were superior to those of other reconstructed methods. Generic-ADMM-Net consists of the reconstructed layers, the noise reduction layers, and the multiplier update layers, as shown in Fig. 4. The role of the noise reduction layers is to estimate and remove artifacts included in the reconstructed layer outputs. The removed artifacts are

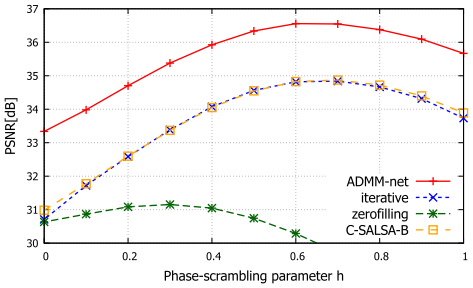

(a) PSNR

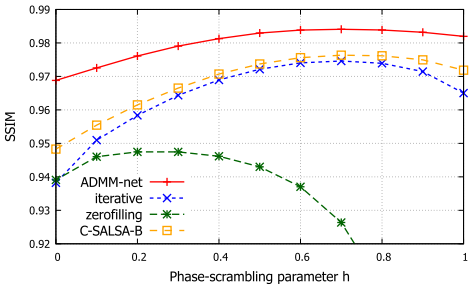

(b) SSIM

FIGURE 10. Quantitative evaluation results of the reconstructed images. In these figures, the phase-scrambling parameter $h = 0$ denotes the results reconstructed from FT signals.

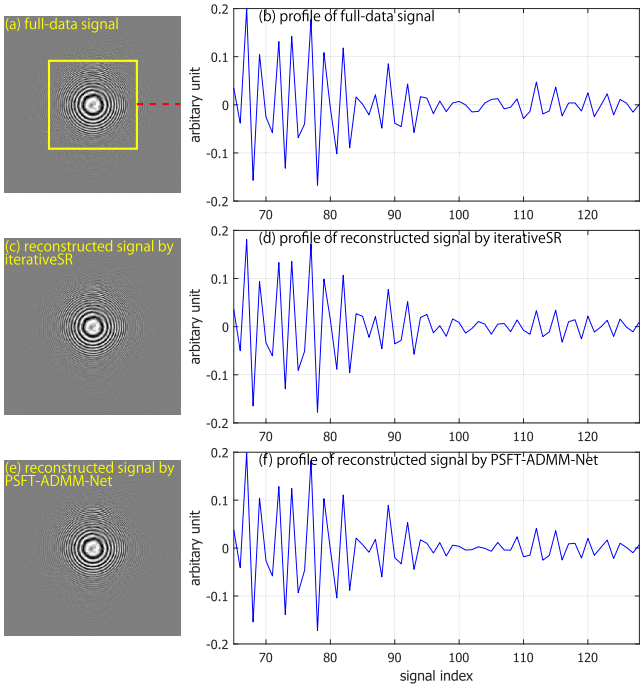

FIGURE 11. Comparison of PSFT signals of reconstructed images shown in Fig. 9. (a), (c), and (e) shows PSFT signals obtained by applying PSFT to the reconstructed images and (b), (d), and (f) shows those profiles. In (a), yellow rectangle indicates the area of under-sampled signal. Signals on red dashed line in (a) are plotted on the profiles.

accumulated in the multiplier update layers. In the reconstructed layers, the reconstructed image is generated from the sum of the ground truth signal and the signal of the noise reduced image. The sum of the ground truth signal and the signal of the noise reduced image behaves as the data consistency and corresponds to the ground truth replacement of the iterative algorithm in previous method. In other words, the data consistency of Generic-ADMM-Net involves the ground truth as well as artifacts to be removed, whereas the previous iterative algorithm simply replaces the ground truth. Therefore, it is considered that the proposed method using Generic-ADMM-Net achieves more effective results than the previous iterative algorithm.

In the experiments with respect to noise-added images, the reconstructed image with the iterative methods, i.e. iterative SR and C-SALSA-B, showed residual noise. The iterative methods are based on replacing the ground truth signal in signal space. If the ground truth signal contains noise, such as in the experimental conditions used here, the reconstructed image also contains residual noise because the ground truth signal containing noise is iteratively replaced in signal space. In other words, it is difficult to remove noise in the reconstruction with the iterative methods. On the other hand, although the reconstructed image with deep-learning, i.e. FT-ADMM-Net and PSFT-ADMM-Net, showed slight smoothing, the noise was almost completely removed. Focusing on the noise reduction layer of Generic-ADMM-Net, this layer consists of 3 sub-layers: two additive layers, two convolution layers, and a nonlinear activation layer, with the outputs of the reconstruction layer and the multiplayer update layer as inputs. The sub-layers of the noise reduction layer have a structure similar to residual learning, such as the Denoising Convolutional Neural Network (DnCNN) [36] proposed by Zhang et al., and have the effect of removing artifacts in the reconstructed image. In this experiment, the training was performed using noise-added images. Therefore, the effect of removing artifacts of the noise reduction layer is also effective in removing the noise added to the images.

On the other hand, Generic-ADMM-Net is different from DnCNN with respect to the object estimated by the network and the ground-truth data for training. Generic-ADMM-Net estimates the reconstructed image and its ground-truth data is a full-data image. DnCNN estimates the residual component, e.g., added noise, because it is easier to optimize the network by estimating only the residual component. Thus, its ground-truth is a noise component. If Generic-ADMM-Net can incorporate residual learning with the noise or artifact component as ground-truth data, like DnCNN, it is expected that this would improve the performance of noise reduction and artifact suppression by the layer $\mathbf{Z}$ in Generic-ADMM-Net

To verify whether the proposed method could be used in MRI in practice, super-resolution simulations of complex images with phase components were conducted. As shown in Fig. 14, it was confirmed that the reconstructed image with PSFT-ADMM-Net was reconstructed without noticeable artifacts such as those in the iterative method, even for complex images. In this experiment, phase estimation was applied to complex images, and the real components of complex images

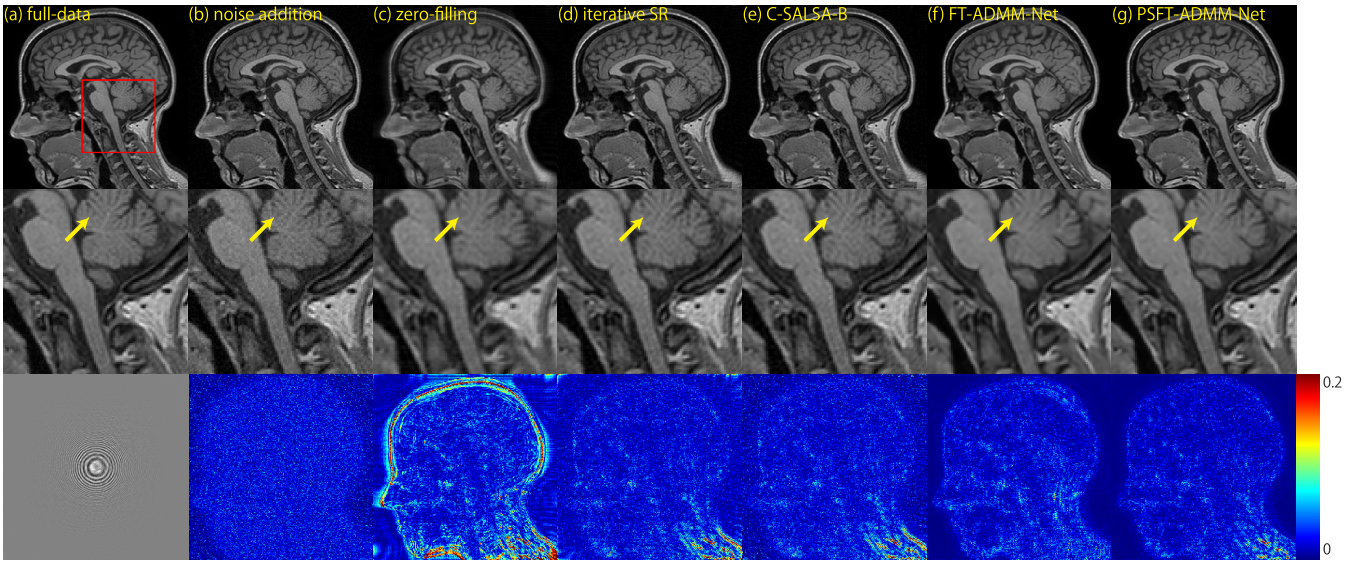

FIGURE 12. Reconstructed images from noise-added T1-weighted images. The noise added to full-data was white Gaussian noise with $\sigma = 0.025$. The top row indicates full-sized reconstructed images, the middle row shows enlarged views of the top row images, and the bottom row shows PSFT signal of full-data and error maps between each reconstructed image and the full data. (d) iterative SR, (e) C-SALSA-B, and (g) PSFT-ADMM-Net are reconstructed from the PSFT signal with $h = 1.0$. (c) zero-filling and (f) FT-ADMM-Net is reconstructed from the FT signal.

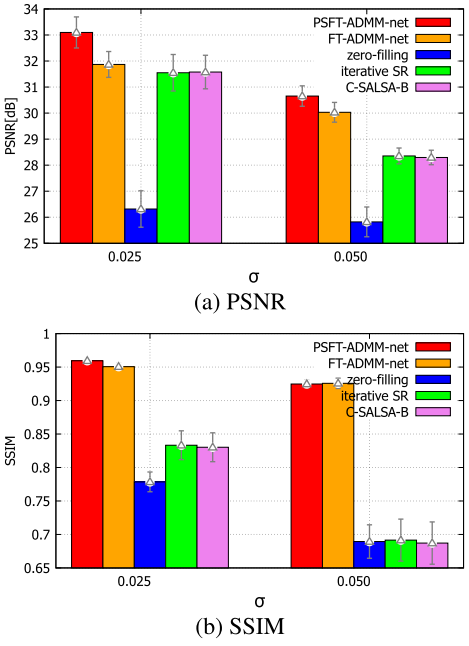

(a) PSNR

(b) SSIM

FIGURE 13. PSNR and SSIM of the reconstructed images from noise-added image.

after phase estimation were treated as real-valued images. As a result, this experiment could be conducted under the condition that the subject could be represented by a real-valued function. On the other hand, the imaginary components of the complex image after phase estimation were used for processing in signal space such as the ground-truth replacement in the iterative methods and the reconstruction layers in Generic-ADMM-Net. The imaginary components are not zero but have low energy. By repeating the ground-truth replacement in the iterative methods, the reconstructed image accumulated information in the imaginary part. Therefore, it was considered that the reconstructed images in the iterative methods have artifacts like texture. In contrast, the reconstruction layer of Generic-ADMM-Net also uses these imaginary components but the reconstructed images have no visible artifacts. Generic-ADMM-Net has the noise reduction layer, and the reconstruction layer uses the noise information derived from the noise reduction layer. Therefore, we believe that Generic-ADMM-Net was able to reconstruct without artifacts.

In addition, we conducted an experiment using the PSFT signal acquired from 0.2T MRI. The model trained by the fastMRI Dataset was used in this experiment. Fig. 15 shows the reconstructed results using PSFT signal acquired from MRI. As shown in Fig. 15, the reconstructed image with the proposed PSFT-ADMM-Net could be reconstructed without artifacts. In addition, there appears to be a slight resolution improvement compared to the zero-filling image. In this experiment, the reconstructed image of PSFT-ADMM-Net was reconstructed using the model trained by using head images in the fastMRI dataset. Because of the different image characteristics of the images used in the test (Yuzu) and those used in the training (head images), it was considered that the resolution improvement of PSFT-ADMM-Net was small. On the other hand, PSFT-ADMM-Net has room to improve the reconstruction results by using images with image features similar to those of the test images for training or by increasing the number of training images.

As other approaches, MR image super-resolution have been proposed for multi-contrast MRI images [45], [46], [47]. These methods are image domain-based super-resolution methods that exploit the relationship between MR images

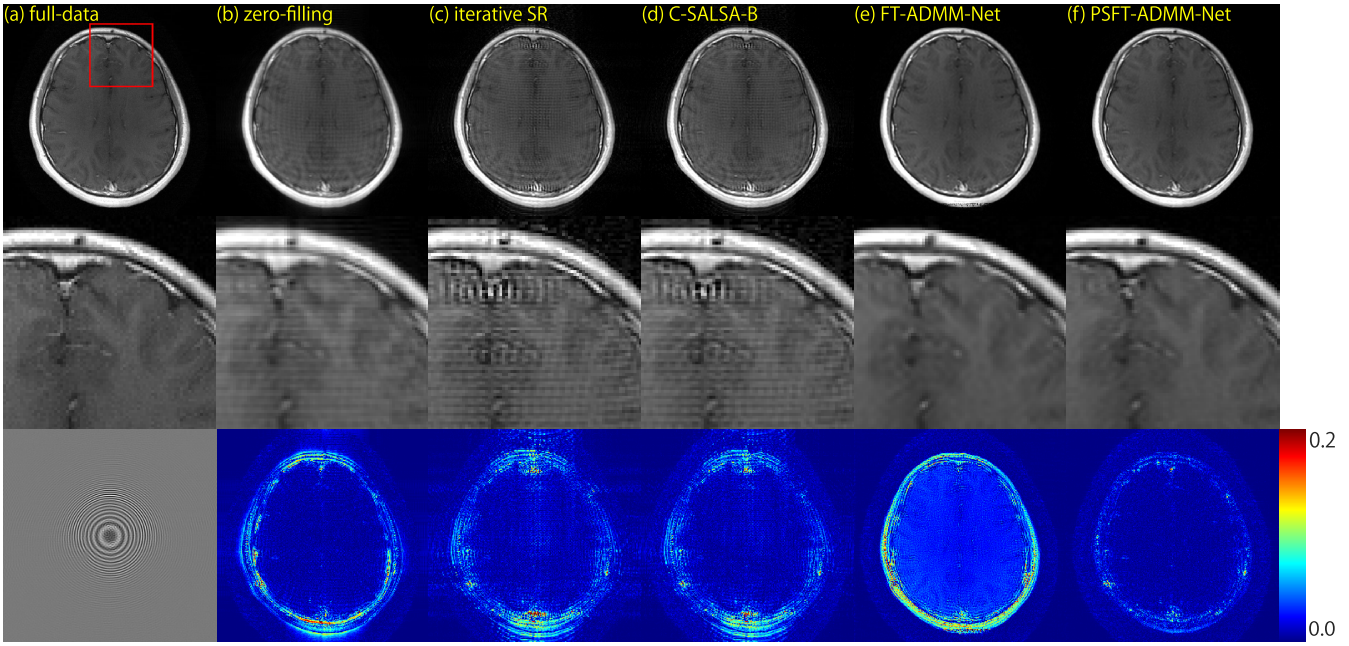

FIGURE 14. Reconstructed images of T1-weighted complex images including phase component. The top row and the middle row show full-sized reconstructed images and enlarged views of red rectangle regions in the full-data, respectively. The bottom row shows the PSFT signal of the full data and error maps between the full data and each reconstructed image. Reconstructed images in (b) and (e) are reconstructed from FT signal. Reconstructed images in (c), (d), and (f) are reconstructed from PSFT signal when $h = 1.0$. Note that the above images have been adjusted for brightness.

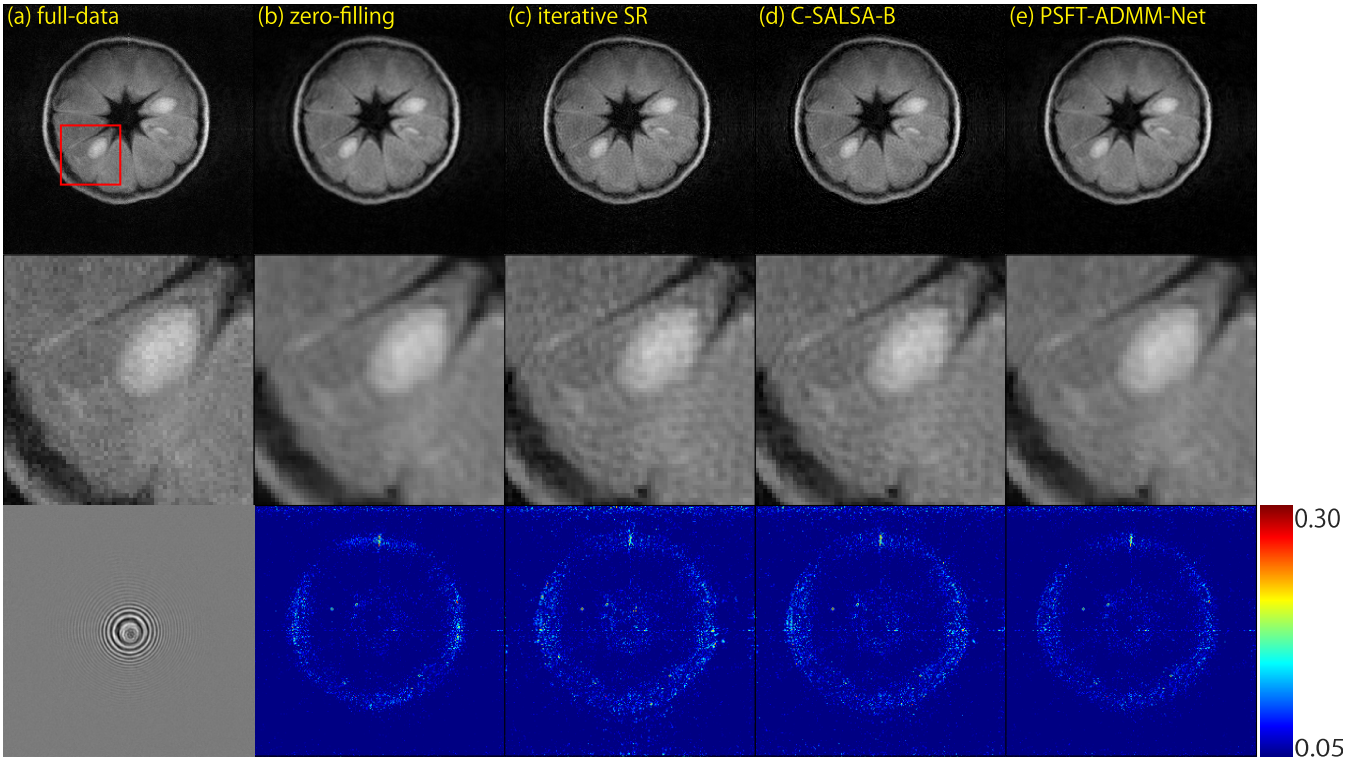

FIGURE 15. Reconstructed images from PSFT signal acquired using 0.2T MRI (Yuzu). The top row and the middle row show full-sized reconstructed images and enlarged views of the red rectangle region in the full data. The bottom row shows the PSFT signal of the full data and error maps between the full data and each reconstructed image, respectively. Reconstructed images are reconstructed from the PSFT signal with $h = 0.8$.

of different contrasts such as T1-weighted and T2-weighted images. On the other hand, the proposed method is a super-resolution method based on the signal domain, and it estimates the high-frequency components from the low-frequency components of the signal to achieve higher resolution. Therefore, the proposed method is a

super-resolution method that is not limited to images with a specific contrast.

To realize PSFT, a quadratic phase modulation must be applied to the spin density function. There are two methods of doing so. One is to add coils that generate a quadratic magnetic field to MRI. This method can acquire a better PSFT signal; however, it requires additional coils and has hardware limitations. The other is to apply the quadratic phase modulation to a radio frequency pulse, and then apply the radio frequency pulse to the gradient magnetic field. The second method has the advantage that it does not require additional devices such as coils and can be applied to existing MRI, although the pulse width of the radio frequency pulses could be wider than the first method.

VII. CONCLUSION

In this paper, a super-resolution method for MR images using a PSFT signal and unrolling-based CNN was proposed. The PSFT signal is effective in improving the resolution under conditions where the target object can be represented by a real-valued function. The feature of the PSFT signal is not found in general-purpose FT imaging for MRI. The proposed method introduced PSFT-compatible Generic-ADMM-Net to image reconstruction since the previous PSFT-based super-resolution algorithm involved iteratively transforming from signal space to image space and vice versa. To verify the effectiveness of the proposed method, simulation experiments were conducted. In measuring the resolution improvement ratio from reconstructed slit images, the reconstruction methods using the PSFT signal including the proposed method improved the resolution of the marginal region. Moreover, the proposed method using a deep-learning technique could improve the resolution of the center region. In the experiments using real-valued MR images, the reconstruction method using the PSFT signal was shown to be more effective for real-valued MR images than zero-filling of the FT signal. To verify the effect with respect to noise-added image, the image reconstruction with the proposed method had a denoising ability derived from the noise reduction layer of Generic-ADMM-Net. In addition, the experiments using complex images with phase components showed that the proposed method did not produce any artifacts in the reconstructed images and that the PSFT signal of the reconstructed images had a small difference from the full-data signal. Furthermore, we demonstrated the reconstruction using the experimentally obtained PSFT signal in order to verify the practical applicability of the proposed method, and the proposed method was shown to be able to reconstruct the experimental PSFT signal with better quality than the iterative methods. Therefore, it was confirmed that the proposed method is highly practical.

ACKNOWLEDGMENT

The authors thank the Information eXtraction from Images project for creating the IXI Dataset and the Center for Advanced Imaging Innovation and Research for providing the fastMRI Dataset.

REFERENCES

[1] E. J. Candes, J. Romberg, and T. Tao, "Robust uncertainty principles: Exact signal reconstruction from highly incomplete frequency information," *IEEE Trans. Inf. Theory*, vol. 52, no. 2, pp. 489–509, Feb. 2006.
[2] D. L. Donoho, "Compressed sensing," *IEEE Trans. Inf. Theory*, vol. 52, no. 4, pp. 1289–1306, Apr. 2006.
[3] M. Lustig, D. Donoho, and J. M. Pauly, "Sparse MRI: The application of compressed sensing for rapid MR imaging," *Magn. Reson. Med.*, vol. 58, no. 6, pp. 1182–1195, 2007.
[4] M. Lustig, D. L. Donoho, J. M. Santos, and J. M. Pauly, "Compressed sensing MRI," *IEEE Signal Process. Mag.*, vol. 25, no. 2, pp. 72–82, Mar. 2008.
[5] U. Gamper, P. Boesiger, and S. Kozerke, "Compressed sensing in dynamic MRI," *Magn. Reson. Med.*, vol. 59, no. 2, pp. 365–373, 2008.
[6] D. Liang, B. Liu, J. Wang, and L. Ying, "Accelerating SENSE using compressed sensing," *Magn. Reson. Med.*, vol. 62, no. 6, pp. 1574–1584, Dec. 2009.
[7] H. Jung, K. Sung, K. S. Nayak, E. Y. Kim, and J. C. Ye, "k-t FOCUSS: A general compressed sensing framework for high resolution dynamic MRI," *Magn. Reson. Med.*, vol. 61, no. 1, pp. 103–116, Jan. 2009.
[8] S. Ito and Y. Yamada, "Alias-free image reconstruction using Fresnel transform in the phase-scrambling Fourier imaging technique," *Magn. Reson. Med.*, vol. 60, no. 2, pp. 422–430, Aug. 2008.
[9] M. Zaitsev, G. Schultz, and J. Hennig, "Extended anti-aliasing reconstruction for phase-scrambled MRI with quadratic phase modulation," in *Proc. ISMRM*, 2009, p. 2859.
[10] J. G. Pipe, "Spatial encoding and reconstruction in MRI with quadratic phase profiles," *Magn. Reson. Med.*, vol. 33, no. 1, pp. 24–33, Jan. 1995.
[11] A. A. Maudsley, "Dynamic range improvement in NMR imaging using phase scrambling," *J. Magn. Reson.*, vol. 76, no. 2, pp. 287–305, Feb. 1988.
[12] V. J. Wedeen, Y.-S. Chao, and J. L. Ackerman, "Dynamic range compression in MRI by means of a nonlinear gradient pulse," *Magn. Reson. Med.*, vol. 6, no. 3, pp. 287–295, Mar. 1988.
[13] G. Puy, J. P. Marques, R. Gruetter, J.-P. Thiran, D. Van De Ville, P. Vandergheynst, and Y. Wiaux, "Spread spectrum magnetic resonance imaging," *IEEE Trans. Med. Imag.*, vol. 31, no. 3, pp. 586–598, Mar. 2012.
[14] Y. Wiaux, G. Puy, R. Gruetter, J.-P. Thiran, D. Van De Ville, and P. Vandergheynst, "Spread spectrum for compressed sensing techniques in magnetic resonance imaging," in *Proc. IEEE Int. Symp. Biomed. Imag., Nano Macro*, Apr. 2010, pp. 756–759.
[15] H. Wang, D. Liang, S. Su, K. F. King, Y. Chang, X. Liu, H. Zheng, and L. Ying, "Improved gradient-echo 3D magnetic resonance imaging using compressed sensing and Toeplitz encoding with phase-scrambled RF excitation," *Med. Phys.*, vol. 47, no. 4, pp. 1579–1589, Apr. 2020.
[16] M. Zaitsev, G. Schultz, J. Hennig, R. Gruetter, and D. Gallichan, "Parallel imaging with phase scrambling," *Magn. Reson. Med.*, vol. 73, no. 4, pp. 1407–1419, Apr. 2015.
[17] S. Ito, S. Yasaka, and Y. Yamada, "MR image reconstruction of a regularly undersampled signal using quadratic phase scrambling," in *Proc. IEEE Int. Conf. Image Process. (ICIP)*, Sep. 2015, pp. 2994–2998.
[18] H. Wang, L. Tam, E. Kopanoglu, D. C. Peters, R. T. Constable, and G. Galiana, "Experimental O-space turbo spin echo imaging," *Magn. Reson. Med.*, vol. 75, no. 4, pp. 1654–1661, Apr. 2016.
[19] S. Ito and Y. Yamada, "Improvement of spatial resolution in magnetic resonance imaging using quadratic phase modulation," in *Proc. 16th IEEE Int. Conf. Image Process. (ICIP)*, Nov. 2009, pp. 2497–2500.
[20] S. Ito and Y. Yamada, "Compressed sensing with super-resolution in magnetic resonance using quadratic phase modulation," in *Proc. Asia Pacific Signal Inf. Process. Assoc. Annu. Summit Conf.*, Dec. 2012, pp. 1–4.
[21] J. P. Stockmann, P. A. Ciris, G. Galiana, L. Tam, and R. T. Constable, "O-space imaging: Highly efficient parallel imaging using second-order nonlinear fields as encoding gradients with no phase encoding," *Magn. Reson. Med.*, vol. 64, no. 2, pp. 447–456, Aug. 2010.
[22] L. K. Tam, G. Galiana, J. P. Stockmann, H. Tagare, D. C. Peters, and R. T. Constable, "Pseudo-random center placement O-space imaging for improved incoherence compressed sensing parallel MRI," *Magn. Reson. Med.*, vol. 73, no. 6, pp. 2212–2224, Jun. 2015.
[23] R. W. Gerchberg, "Super-resolution through error energy reduction," *Optica Acta, Int. J. Opt.*, vol. 21, no. 9, pp. 709–720, Sep. 1974.

[24] L. Yue, H. Shen, J. Li, Q. Yuan, H. Zhang, and L. Zhang, "Image super-resolution: The techniques, applications, and future," *Signal Process.*, vol. 128, pp. 389–408, Nov. 2016.
[25] H. Chen, X. He, L. Qing, Y. Wu, C. Ren, R. E. Sheriff, and C. Zhu, "Real-world single image super-resolution: A brief review," *Inf. Fusion*, vol. 79, pp. 124–145, Mar. 2022.
[26] S. Farsiu, D. Robinson, M. Elad, and P. Milanfar, "Advances and challenges in super-resolution," *Int. J. Imag. Syst. Technol.*, vol. 14, no. 2, pp. 47–57, 2004.
[27] Y. Yang, J. Sun, H. Li, and Z. Xu, "ADMM-CSNet: A deep learning approach for image compressive sensing," *IEEE Trans. Pattern Anal. Mach. Intell.*, vol. 42, no. 3, pp. 521–538, Mar. 2020.
[28] K. Hammernik, T. Klatzer, E. Kobler, M. P. Recht, D. K. Sodickson, T. Pock, and F. Knoll, "Learning a variational network for reconstruction of accelerated MRI data," *Magn. Reson. Med.*, vol. 79, no. 6, pp. 3055–3071, 2018.
[29] J. Zhang and B. Ghanem, "ISTA-Net: Interpretable optimization-inspired deep network for image compressive sensing," in *Proc. IEEE/CVF Conf. Comput. Vis. Pattern Recognit.*, Jun. 2018, pp. 1828–1837.
[30] H. K. Aggarwal, M. P. Mani, and M. Jacob, "MoDL: Model-based deep learning architecture for inverse problems," *IEEE Trans. Med. Imag.*, vol. 38, no. 2, pp. 394–405, Feb. 2019.
[31] J. Schlemper, J. Caballero, J. V. Hajnal, A. N. Price, and D. Rueckert, "A deep cascade of convolutional neural networks for dynamic MR image reconstruction," *IEEE Trans. Med. Imag. (TMI)*, vol. 37, no. 2, pp. 491–503, Feb. 2018.
[32] O. Ronneberger, P. Fischer, and T. Brox, "U-Net: Convolutional networks for biomedical image segmentation," in *Medical Image Computing and Computer-Assisted Intervention—MICCAI*. Munich, Germany: Springer, 2015, pp. 234–241.
[33] G. Yang, S. Yu, H. Dong, G. Slabaugh, P. L. Dragotti, X. Ye, F. Liu, S. Arridge, J. Keegan, Y. Guo, and D. Firmin, "DAGAN: Deep de-aliasing generative adversarial networks for fast compressed sensing MRI reconstruction," *IEEE Trans. Med. Imag.*, vol. 37, no. 6, pp. 1310–1321, Jun. 2018.
[34] I. Goodfellow, J. Pouget-Abadie, M. Mirza, B. Xu, D. Warde-Farley, S. Ozair, A. Courville, and Y. Bengio, "Generative adversarial networks," *Commun. ACM*, vol. 63, no. 11, pp. 139–144, 2020.
[35] S. Wang, Z. Su, L. Ying, X. Peng, S. Zhu, F. Liang, D. Feng, and D. Liang, "Accelerating magnetic resonance imaging via deep learning," in *Proc. IEEE 13th Int. Symp. Biomed. Imag. (ISBI)*, Apr. 2016, pp. 514–517.
[36] K. Zhang, W. Zuo, Y. Chen, D. Meng, and L. Zhang, "Beyond a Gaussian denoiser: Residual learning of deep CNN for image denoising," *IEEE Trans. Image Process.*, vol. 26, no. 7, pp. 3142–3155, Jul. 2017.
[37] D. Gabay and B. Mercier, "A dual algorithm for the solution of nonlinear variational problems via finite element approximation," *Comput. Optim. Appl.*, vol. 2, no. 1, pp. 17–40, 1976.
[38] J. Eckstein and D. P. Bertsekas, "On the douglas—Rachford splitting method and the proximal point algorithm for maximal monotone operators," *Math. Program.*, vol. 55, nos. 1–3, pp. 293–318, Apr. 1992.
[39] *IXI Dataset*. Accessed: Jun. 1, 2023. [Online]. Available: https://brain-development.org/ixi-dataset/
[40] *fastMRI Dataset*. Accessed: Jun. 1, 2023. [Online]. Available: https://fastmri.med.nyu.edu/
[41] V. Nair and G. E. Hinton, "Rectified linear units improve restricted Boltzmann machines," in *Proc. 27th Int. Conf. Mach. Learn.*, 2010, pp. 807–814.
[42] D. P. Kingma and J. Ba, "Adam: A method for stochastic optimization," 2014, *arXiv:1412.6980*.
[43] Z. Wang, A. C. Bovik, H. R. Sheikh, and E. P. Simoncelli, "Image quality assessment: From error visibility to structural similarity," *IEEE Trans. Image Process.*, vol. 13, no. 4, pp. 600–612, Apr. 2004.
[44] Y. Liu, J.-F. Cai, Z. Zhan, D. Guo, J. Ye, Z. Chen, and X. Qu, "Balanced sparse model for tight frames in compressed sensing magnetic resonance imaging," *PLoS ONE*, vol. 10, no. 4, Apr. 2015, Art. no. e0119584.
[45] H. Zheng, K. Zeng, D. Guo, J. Ying, Y. Yang, X. Peng, F. Huang, Z. Chen, and X. Qu, "Multi-contrast brain MRI image super-resolution with gradient-guided edge enhancement," *IEEE Access*, vol. 6, pp. 57856–57867, 2018.
[46] Q. Lyu, H. Shan, C. Steber, C. Helis, C. Whitlow, M. Chan, and G. Wang, "Multi-contrast super-resolution MRI through a progressive network," *IEEE Trans. Med. Imag.*, vol. 39, no. 9, pp. 2738–2749, Sep. 2020.
[47] G. Li, J. Lv, Y. Tian, Q. Dou, C. Wang, C. Xu, and J. Qin, "Transformer-empowered multi-scale contextual matching and aggregation for multi-contrast MRI super-resolution," in *Proc. IEEE/CVF Conf. Comput. Vis. Pattern Recognit. (CVPR)*, Jun. 2022, pp. 20604–20613.

KAZUKI YAMATO (Member, IEEE) received the B.E., M.E., and Ph.D. degrees from Utsunomiya University, in 2009, 2011, and 2014, respectively. He was a Postdoctoral Researcher with Utsunomiya University, from 2014 to 2016. He was a Postdoctoral Researcher with the Department of Information Science, Tohoku Gakuin University, from 2016 to 2017. He was a Postdoctoral Researcher with Gunma University, from 2017 to 2018. He was a Project Assistant Professor with Gunma University, from 2018 to 2020. He has been a Research Associate with Utsunomiya University, since April 2020. His research interests include data hiding, image processing, audio signal processing, and application of tunable focus lens.

SATOSHI ITO (Member, IEEE) received the B.E. and M.E. degrees from the Department of Electrical Engineering, Utsunomiya University, in 1987 and 1989, respectively, and the Ph.D. degree from Utsunomiya University, in 2001. He has been a Professor with the Department of Information Science, Utsunomiya University, since 2012. He joined Toshiba Company. His research interests include MR high-speed imaging techniques using compressed sensing and deep learning, and image reconstruction and image processing methods. He is a member of the International Society of Magnetic Resonance in Medicine (ISMRM), the Japanese Society for Magnetic Resonance in Medicine (JSMRM), and the Japanese Society of Medical Imaging Technology.